

Plasmonic photonic crystal with a complete band gap for surface plasmon polariton waves

Liang Feng,^{1,a)} Ming-Hui Lu,² Vitaliy Lomakin,¹ and Yeshaiahu Fainman¹

¹Department of Electrical and Computer Engineering, University of California, San Diego, La Jolla, California 92093, USA

²National Laboratory of Solid State Microstructures, Nanjing University, Jiangsu 210093, People's Republic of China

(Received 23 September 2008; accepted 17 November 2008; published online 9 December 2008)

A dielectric plasmonic photonic crystal for manipulating surface plasmon polariton (SPP) fields has been designed, fabricated, and tested. The band structure of SPP fields inside the plasmonic photonic crystal has been calculated using the plane wave expansion method and validated by full wave numerical simulations. The fabricated device was characterized using our far-field SPP imaging technique. The transmittance of incident SPP waves is about 5% at 1520 nm (a designed band gap frequency), confirming the designed band structure. The results show, both experimentally and theoretically, a complete two-dimensional band gap for in-plane SPP waves. The SPP fields at frequencies within this specified $0.14\omega a/2\pi c$ -wide band gap frequency range are forbidden to propagate through the plasmonic photonic crystal. © 2008 American Institute of Physics. [DOI: 10.1063/1.3043581]

Surface plasmon polaritons (SPPs) are electromagnetic surface waves formed through strong interaction between optical electromagnetic fields and electron density oscillations on a metal-dielectric interface. One of the unique SPP properties is that their wavelength can be shorter than the wavelength of optical field in the surrounding dielectric media, leading to applications relying on subdiffraction-limited resolution.¹⁻³ However, excitation and control of SPP fields have not yet been advanced in a systematic fashion as, for example, for optical fields in free space. Recent work on Fourier plasmonics starts exploiting both refractive^{4,5} and diffractive^{6,7} SPP devices. Moreover, SPP fields can be excited and manipulated by photonic crystal lattices (PCLs) similar to that of light in photonic crystals made of dielectrics. For example, due to Bragg resonance at the boundaries of Brillouin zones, the SPP fields in a specified frequency range are forbidden to propagate through a periodic array of in-plane metallic bumps, which has been used to make waveguides with subwavelength confinement,^{8,9} high-efficiency Bragg reflectors,¹⁰ and resonators¹¹ for SPP fields. However, it is difficult, if possible, to analytically calculate the band structure of these metallic plasmonic photonic crystals (PPCs) using conventional methods such as the plane

wave expansion (PWE) method¹² and the multiple scattering theory.¹³ In this letter, we introduce a metallodielectric PPC, where the PCL is implemented in the dielectric material on the metal-dielectric interface. The band structure of the PPC has been theoretically calculated using the PWE method, exhibiting a complete wide two-dimensional (2D) band gap for SPP fields. The experimental testing and numerical simulations of such a fabricated device confirm the band structure, validating our approach.

Figure 1(a) shows the structural geometry of our PPC design consisting of a 2D array of high dielectric constant Si cylinders surrounded by low dielectric constant air on the surface of Al. The Si cylinders are 200 nm in diameter and 400 nm in height, and they are arranged in a square mesh with a lattice constant of $a=500$ nm. Since Si-Al and air-Al interfaces have different effective indices for in-plane SPP waves, the equivalent potential diagram in quantum mechanics would correspond to an electron propagating in a real crystal or light propagating in photonic crystals. This periodic potential contrast can cause strong scatterings near the boundaries of Brillouin zones, thus modifying SPP's dispersion and resulting in a complete band gap caused by Bragg resonances. For experimental validation, we integrate the

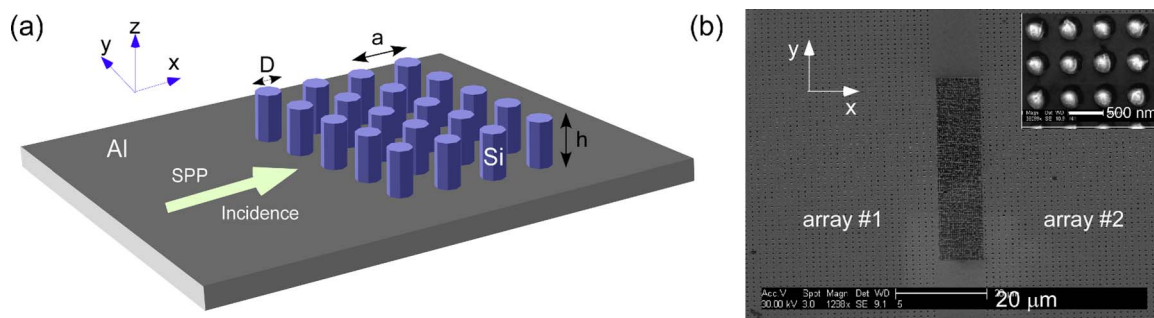


FIG. 1. (Color online) (a) Schematic of PPC's geometry with design parameters of $a=500$ nm, $D=200$ nm, and $h=400$ nm. (b) SEM micrographs of the integrated structure consisting of nanohole array 1, a PPC, and nanohole array 2.

^{a)}Electronic mail: lifeng@ucsd.edu.

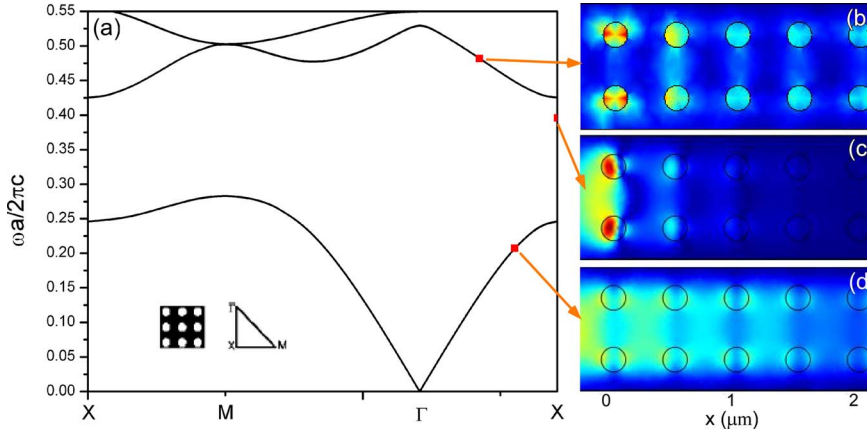


FIG. 2. (Color online) (a) Calculated band structure of the proposed PPC using the PWE method with 289 plane waves. A $0.14\omega a/2\pi c$ -wide 2D complete band gap can be observed from $0.28\omega a/2\pi c$ to $0.42\omega a/2\pi c$. Full wave 3D finite element simulations show $|H_y|$ of SPP waves propagating inside the proposed PPC at different frequencies. (b) $0.48\omega a/2\pi c$ (corresponding to the 2nd band). (c) $0.39\omega a/2\pi c$ (corresponding to the band gap). (d) $0.22\omega a/2\pi c$ (corresponding to the first band).

PPC with two 2D nanohole arrays on a single “chip” for excitation and detection as discussed in Ref. 6 [see Fig. 1(b)]. The chip consists of a pair of 2D nanohole arrays and the PPC between them. Nanohole array 1 will allow to excite SPP fields that will be incident onto the PPC and the transmitted SPP field will be scattered by array 2 into free space for detection and assessment of the PPC properties.

For propagating SPP waves along the x direction (see Fig. 1), there are three field components, E_x , H_y , and E_z , which can be expressed as

$$E = E_0 \begin{pmatrix} jk_z/k_x \\ 0 \\ 1 \end{pmatrix} \exp(-jk_x x - k_z z), \quad (1)$$

$$H = -\frac{E_0 \omega \varepsilon(r) \mu_0}{k_x} \begin{pmatrix} 0 \\ 1 \\ 0 \end{pmatrix} \exp(-jk_x x - k_z z), \quad (2)$$

where $k_x = k_{\text{SPP}} = k_0 \sqrt{\varepsilon_m \varepsilon(r) / [\varepsilon_m + \varepsilon(r)]}$, $k_z = \sqrt{k_x^2 - \varepsilon(r) k_0^2}$, and ε_m and $\varepsilon(r)$ are permittivities of Al and air (or Si), respectively. These electric and magnetic field components are not independent as the eigenstate for one component is also the eigenstate for the other two components. Due to the boundary continuity, the E_z component has been chosen to form eigenfunctions and used to calculate the band structure of the PPC using the PWE method. Since most of SPP's energy is confined on the surface, it is therefore reasonable to simplify Eq. (1) to consider E_z at $z=0$,

$$E_z(r) = E_0 \exp(-jk_{\text{SPP}} r). \quad (3)$$

For in-plane SPP propagation, as reported in Refs. 6 and 7, the effective wavevector can be expressed as k_{SPP} with the still valid Helmholtz equation

$$\frac{1}{\varepsilon_{\text{SPP}}(r)} \left(\frac{\partial^2}{\partial x^2} + \frac{\partial^2}{\partial y^2} \right) E_z(r) = \frac{\omega^2}{c^2} E_z(r), \quad (4)$$

where $\varepsilon_{\text{SPP}}(r) = (k_{\text{SPP}}/k_0)^2 = \varepsilon_m \varepsilon(r) / [\varepsilon_m + \varepsilon(r)]$. By expanding $E_z(r)$ and $\varepsilon_{\text{SPP}}(r)$ in reciprocal space using Bloch theory, the eigenfunction of our PPC can be derived as

$$\sum_{\vec{G}} \varepsilon_{\text{SPP}}^r (|\vec{G} - \vec{G}'|) |\vec{k} + \vec{G}| |\vec{k} + \vec{G}'| E_z(\vec{G}) = \frac{\omega^2}{c^2} E_z(\vec{G}). \quad (5)$$

For simplicity, we use Drude model for the permittivity of Al and since the band structure is only determined by the real

part of the permittivities,¹⁴ we do not consider the imaginary part of the permittivity ($\varepsilon_m = 1 - \omega_p^2/\omega^2$, where the plasma frequency ω_p is 2.24×10^{16} rad/s).¹⁵ The permittivities of air and Si are set 1 and 12.4, respectively. The calculated band diagram [see Fig. 2(a)] shows a complete $0.14\omega a/2\pi c$ -wide 2D band gap from $0.28\omega a/2\pi c$ to $0.42\omega a/2\pi c$. The complete 2D band gap results from high contrast between air and Si cylinders in $\varepsilon_{\text{SPP}}(r)$.

This band structure is next validated by full wave three-dimensional (3D) finite element simulations (with 400 nm high Si cylinders on the Al surface) using COMSOL MULTIPHYSICS 3.4, as shown in Figs. 2(b)–2(d). A SPP wave, propagating from left to right, is launched at the left side of the simulation region. The periodic boundary condition is implemented in the vertical direction and the perfect matched layer boundary condition is applied on all other boundaries to eliminate the reflection. The permittivity of Al is still described by the Drude model ($\varepsilon_m = 1 - \omega_p^2/\omega(\omega - j\gamma)$) but with a damping coefficient of $\gamma = 1.22 \times 10^{14}$ rad/s.¹⁵ We observe [see Figs. 2(b) and 2(d)] that the SPP wave can propagate inside the PPC in the second and the first bands at the frequencies of $0.48\omega a/2\pi c$ and $0.22\omega a/2\pi c$. However, in the band gap occurring at the frequency of $0.39\omega a/2\pi c$ [see Fig. 2(c)], strong attenuation can be observed and the SPP field propagation is forbidden.

We fabricated the sample with the following steps: (i) a glass substrate was cleaned and coated with 5 nm thick Ti and 100 nm thick Al films; (ii) a 1.5 μm thick polymethyl methacrylate (PMMA) layer was spun onto the Al plate and the designed PPC features were defined in PMMA by direct E-beam writing; (iii) 400 nm thick amorphous Si was deposited over the PMMA mask; (iv) using acetone lift-off, the PMMA mask was removed, forming the designed Si-based PPC on the Al film surface; (v) the entire sample was then covered again with a 200 nm thick PMMA layer for the fabrication of two nanohole arrays, 1 to the left and 2 to the right of the PPC; (vi) the PMMA was e-beam patterned to create $100 \times 100 \mu\text{m}^2$ nanohole arrays consisting of nanoholes with a diameter of about 300 nm on a 1.6 μm period square grid; (vii) the nanohole arrays were transferred to the Al film by wet chemical etching and PMMA was then removed using acetone. The SEM micrograph of the Si-based PPC on the Al film is reproduced in the inset of Fig. 1(b).

The fabricated PPC consists of 20 and 80 lattice elements in the longitudinal and the transverse directions of the propagating SPP field, respectively. The integrated device was characterized using our far-field SPP detection system at

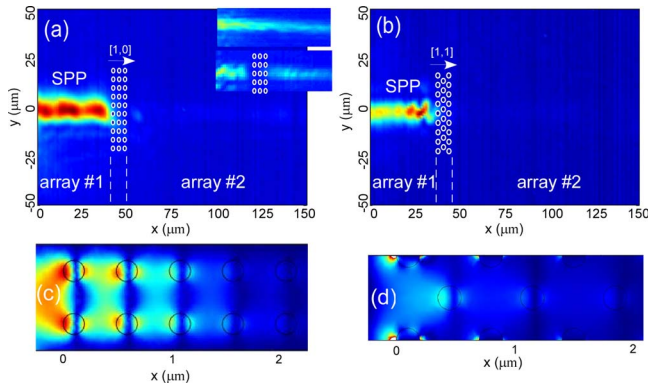


FIG. 3. (Color online) [(a) and (b)] Measured SPP time-averaged intensity maps as the SPP field is excited in nanohole array 1, propagates through the PPC, and the transmitted SPP scatters from nanohole array 2 at 1520 nm ($0.33\omega a/2\pi c$). [(c) and (d)] Numerical mappings of $|H_y|$ of SPP waves propagating inside the proposed PPC at $0.33\omega a/2\pi c$. The SPP waves are incident along the PPC's lattice orientations: [(a) and (c)] $[1, 0]$ and [(b) and (d)] $[1, 1]$. The insets in (a) represent the unperturbed SPP propagation on a continuous nanohole array (top) and propagation through a PPC with $a = 1000$ nm (the working wavelength is located in the first band) (bottom).

the wavelength of 1520 nm ($0.33\omega a/2\pi c$).^{6,16,17} Incident light used for excitation of SPP waves in nanohole array 1 was polarized at 45° in the Cartesian coordinate system of the nanohole array grid. The SPP field transmitted through the PPC was radiated on nanohole array 2 and the scattered free space modes were transmitted through an orthogonally oriented polarization analyzer and imaged by a lens onto a charge coupled device camera for detection and analysis.

Figures 3(a) and 3(b) show the measured SPP time-averaged intensity maps as the SPP field is excited in nanohole array 1, propagates through the PPC, and the transmitted SPP scatters from nanohole array 2 (see the labeled regions). The width of the excited SPP beam is about $10 \mu\text{m}$ and its convergence is controlled within a half angle of 2° . Note that the SPP excitation spot in nanohole array 1 is not in the field of view of the images shown in Figs. 3(a) and 3(b) (i.e., the excited SPP waves enter the left boundaries on the images). The PPCs in Figs. 3(a) and 3(b) are fabricated for operation with normally incident SPP fields to propagate along $[1, 0]$ (Γ -X) and $[1, 1]$ (Γ -M) orientations of the PPC lattices, respectively. Since the ratio between the measured out-coupled intensities can represent the ratio between SPP energies at different spots,¹⁸ we calculated, from the experimental data, the ratio between out-coupled SPP intensities at two spots, right before and after the PPC, to evaluate the transmission coefficients. The measured transmittances are about 5.4% and 5.8%, respectively, which are about six times less than the transmittance observed with a 400 nm high Si slab on an Al surface.⁶ To have visual comparisons, the insets in Fig. 3(a) show the image of unperturbed SPP propagation on a continuous nanohole array (top) and the SPP's transmission through the first passing band of another PPC with $a = 1000$ nm. For both PPC orientations shown in Figs. 3(a) and 3(b), the incident SPP waves cannot propagate through the PPC since the wavelength of 1520 nm ($0.33\omega a/2\pi c$) lies within the complete band gap of the PPC, as expected from Fig. 2(a). Numerical simulations in Figs. 3(c) and 3(d) also confirm our measured results, showing strong attenuation inside the PPC for both lattice orientations. However, it should be noted that compared to numerical simulation at

$0.39\omega a/2\pi c$ [see Fig. 2(c)], the SPP fields at $0.33\omega a/2\pi c$ decay slower [see Fig. 3(c)], although the value $0.33\omega a/2\pi c$ lies closer to PPC's midgap frequency. This might be due to lower effective index caused by finite height of Si cylinders that is about four times shorter than the SPP's evanescent tail extending into the dielectric medium. Lower effective index can cause blueshift of PPC's band structure.

In summary, a PPC, which can modulate the propagation of in-plane SPP waves, has been designed, fabricated, and validated experimentally. The band structure has been calculated using the PWE method with proper approximations. It shows a complete $0.14\omega a/2\pi c$ -wide 2D band gap. This complete band gap is verified by full wave 3D numerical simulations using the actual geometry of the fabricated device and confirmed by experimental characterizations. In the future, our metallodielectric approach to PPC with an appropriate design of the desired band structure will allow more accurate design and realization of PPC-based on-chip waveguides, reflectors, and resonators. In addition, numerous phenomena that have been observed in conventional dielectric photonic crystals, including superprism,¹⁹ self-collimation,²⁰ and negative refraction²¹ can be also demonstrated for SPP waves.

This work was supported by DARPA Center for Optofluidic Integration and NSF.

¹H. Raether, *Surface Plasmons on Smooth and Rough Surfaces and on Gratings* (Springer, Berlin, 1988), pp. 4–7.

²W. L. Barnes, A. Dereux, and T. W. Ebbesen, *Nature (London)* **424**, 824 (2003).

³E. Ozbay, *Science* **311**, 189 (2006).

⁴A. Hohenau, J. R. Krenn, A. L. Stepanov, A. Drezet, H. Ditlbacher, B. Steinberger, A. Leitner, and F. R. Aussenegg, *Opt. Lett.* **30**, 893 (2005).

⁵B. Steinberger, A. Hohenau, H. Ditlbacher, F. R. Aussenegg, A. Leitner, and J. R. Krenn, *Appl. Phys. Lett.* **91**, 081111 (2007).

⁶L. Feng, K. A. Tetz, B. Slutsky, V. Lomakin, and Y. Fainman, *Appl. Phys. Lett.* **91**, 081101 (2007).

⁷R. Zia and M. L. Brongersma, *Nat. Nanotechnol.* **2**, 426 (2007).

⁸S. I. Bozhevolnyi, J. E. Erland, K. Leosson, P. M. W. Skovgaard, and J. M. Hvam, *Phys. Rev. Lett.* **86**, 3008 (2001).

⁹C. Marquart, S. I. Bozhevolnyi, and K. Leosson, *Opt. Express* **13**, 3303 (2005).

¹⁰M. U. Gonzalez, J. C. Weeber, A. L. Baudrion, A. Dereux, A. L. Stepanov, J. R. Krenn, E. Devaux, and T. W. Ebbesen, *Phys. Rev. B* **73**, 155416 (2006).

¹¹J. C. Weeber, A. Bouhelier, G. Colas des Francs, L. Markey, and A. Dereux, *Nano Lett.* **7**, 1352 (2007).

¹²K. M. Ho, C. T. Chan, and C. M. Soukoulis, *Phys. Rev. Lett.* **65**, 3152 (1990).

¹³X. Zhang, Z. Q. Zhang, L. M. Li, C. Jin, D. Zhang, B. Man, and B. Cheng, *Phys. Rev. B* **61**, 1892 (2000).

¹⁴L. Feng, X. P. Liu, Y. F. Tang, Y. F. Chen, J. Zi, S. N. Zhu, and Y. Y. Zhu, *Phys. Rev. B* **71**, 195106 (2005).

¹⁵I. El-Kady, M. M. Sigalas, R. Biswas, K. M. Ho, and C. M. Soukoulis, *Phys. Rev. B* **62**, 15299 (2000).

¹⁶K. A. Tetz, R. Rokitski, M. Nezhad, and Y. Fainman, *Appl. Phys. Lett.* **86**, 111110 (2005).

¹⁷R. Rokitski, K. A. Tetz, and Y. Fainman, *Phys. Rev. Lett.* **95**, 177401 (2005).

¹⁸K. A. Tetz, R. Rokitski, M. Nezhad, and Y. Fainman, in *Proceedings of the IEEE LEOS Annual Meeting 2004*, Rio Grande, Puerto Rico (IEEE, New York, 2004).

¹⁹H. Kosaka, T. Kawashima, A. Tomita, M. Notomi, T. Tamamura, T. Sato, and S. Kawakami, *Phys. Rev. B* **58**, R10096 (1998).

²⁰H. Kosaka, T. Kawashima, A. Tomita, M. Notomi, T. Tamamura, T. Sato, and S. Kawakami, *Appl. Phys. Lett.* **74**, 1212 (1999).

²¹E. Cubukcu, K. Aydin, E. Ozbay, S. Foteinopoulou, and C. M. Soukoulis, *Nature (London)* **423**, 604 (2003).